

The ROSAT Deep Survey

I. X-ray sources in the Lockman Field

G. Hasinger¹, R. Burg², R. Giacconi³, M. Schmidt⁴, J. Trümper⁵, G. Zamorani^{6,7}

¹ Astrophysikalisches Institut Potsdam, An der Sternwarte 16, 14482 Potsdam, Germany

² Johns Hopkins University, Baltimore, MD 21218, USA

³ European Southern Observatory, Karl-Schwarzschild-Str. 1, 85748 Garching bei München, Germany

⁴ California Institute of Technology, Pasadena, CA 91125, USA

⁵ Max-Planck-Institut für extraterrestrische Physik, Karl-Schwarzschild-Str. 2, 85740 Garching bei München, Germany

⁶ Istituto di Radioastronomia del CNR, via Gobetti 101, I-40129 Bologna, Italy

⁷ Osservatorio Astronomico, via Zamboni 33, I-40126 Bologna, Italy

Received 12 May 1997; accepted 4 Aug 1997

Abstract. The ROSAT Deep Survey in the *Lockman Hole* is the most sensitive X-ray survey performed to date, encompassing an exposure time of 207 ksec with the PSPC and a total of 1.32 Msec with the HRI aboard ROSAT. Here we present the complete catalogue of 50 X-ray sources with PSPC fluxes (0.5–2 keV) above $5.5 \times 10^{-15} \text{ erg cm}^{-2} \text{ s}^{-1}$. The optical identifications are discussed in an accompanying paper (Schmidt et al., 1997). We also derive a new $\log(N)$ – $\log(S)$ function reaching a source density of $970 \pm 150 \text{ deg}^{-2}$ at a limiting flux of $10^{-15} \text{ erg cm}^{-2} \text{ s}^{-1}$. At this level 70–80% of the 0.5–2 keV X-ray background is resolved into discrete sources. Utilizing extensive simulations of artificial PSPC and HRI fields we discuss in detail the effects of source confusion and incompleteness both on source counts and on optical identifications. Based on these simulations we set conservative limits on flux and on off-axis angles, which guarantee a high reliability of the catalogue. We also present simulations of shallower fields and show that surveys, which are based on PSPC exposures longer than 50 ksec, become severely confusion limited typically a factor of 2 above their 4σ detection threshold. This has consequences for recent claims of a possible new source population emerging at the faintest X-ray fluxes.

Key words: surveys – cosmology: diffuse radiations – X-rays: galaxies

1. Introduction

The study of the X-ray background (XRB), originally discovered 35 years ago (Giacconi et al., 1962), with imaging X-ray telescopes has progressed rapidly in the last few years. After a pioneering start with deep Einstein exposures (Giacconi et al., 1979, Griffiths et al., 1983, Hamilton et al., 1991), ROSAT deep survey observations were able to resolve the majority of the soft XRB into discrete sources (Hasinger et al., 1993, hereafter H93). First deep imaging exposures with ASCA have extended these studies into the hard X-ray band (Inoue et al. 1996, Cagnoni et al., 1997). The X-ray band is one of the few regions of the electromagnetic spectrum, where the integrated emission of discrete sources, summed over all cosmic epochs, is dominating the celestial emission. The XRB therefore provides a strong constraint for cosmological evolution models (see e.g. Comastri et al., 1995; Zdziarski 1996). In order to understand the populations contributing to the X-ray background and their cosmological evolution it is necessary to obtain complete optical identification of the sources detected in X-ray deep surveys. The majority of optically identified X-ray sources at faint fluxes are active galactic nuclei (AGN), i.e. QSOs and Seyfert galaxies with broad emission lines (Shanks et al., 1991; Boyle et al., 1993; Bower et al., 1996; Page et al., 1996). Using the large samples of X-ray selected AGN now becoming available, their luminosity function and its evolution with redshift can be studied in detail (Boyle et al., 1995; Page et al., 1996; Jones et al., 1996). The current models, which are based on pure luminosity evolution, predict that the broad-line AGN contribute only 30–50% to the soft X-ray background and much less to the hard X-ray background. Postulating a large population of faint, intrinsically ab-

sorbed AGN, some models predict a much larger fraction of the soft XRB, and possibly all of the hard XRB as due to AGN (see e.g. Comastri et al., 1995; Zdziarski 1996).

There are, however, reports that at the faintest X-ray fluxes a new population of X-ray active, but optically relatively normal narrow-emission line galaxies (NELG) start to dominate the X-ray counts, and could ultimately contribute the majority of the XRB (Georgantopoulos et al. 1996, Griffiths et al. 1996, McHardy et al., 1997). These claims are based on deep ROSAT PSPC surveys which – as we will show – start to be severely confusion limited at the faintest fluxes. Care has therefore to be taken to assess the systematic position errors and misidentification likelihood at faint fluxes. In our own deep survey identification work we have therefore taken measures to minimize confusion and to increase the reliability of the X-ray catalogue. We restricted the sample to X-ray fluxes well above the detection threshold at a reliable flux level derived from detailed simulations. Secondly, we invested massive amounts of ROSAT HRI time to cover our deepest survey field in the Lockman Hole, this way minimizing position errors and confusion. In this paper (paper I) we describe the derivation of the X-ray source catalogue in the Lockman Hole. Section 2 gives a summary of the observations, Sect. 3 describes the new maximum likelihood (ML) crowded-field detection algorithm developed for deep X-ray survey work, Sect. 4 discusses the necessary astrometric corrections for ROSAT PSPC and HRI images and Sect. 5 gives the final source catalogue. The verification of the analysis procedure through simulations and the derivation of a final $\log(N)$ – $\log(S)$ function are discussed in Sect. 6 and a discussion of the results is given in Sect. 7. The complete optical identification of the X-ray source catalogue is described in *paper II* (Schmidt et al., 1997) and deep VLA radio observations of the field are discussed by deRuiter et al. (1997).

2. Observations

The data presented here consists of all observations of the ROSAT Deep Survey accumulated in the period 1990–1997 in the direction of the Lockman Hole, which is one of the areas on the sky with a minimum of the galactic Hydrogen column density; N_H is roughly $5 \times 10^{19} \text{ cm}^{-2}$ in this field (Lockman et al., 1986). Table 1 gives a summary of these observations. Specifically, a total exposure time of 207.41 ksec was accumulated with PSPC (Pfeffermann and Briel 1992) pointings centered at the direction $RA(2000) = 10^h52^m$, $DEC(2000) = 57^\circ21'36''$. These data have been partially presented in H93. For the PSPC data all good time intervals selected by the ROSAT standard analysis (SASS; Voges 1992) have been analysed. The individual datasets obtained in different semesters, which are affected by residual erratic aspect errors of order 10 arcsec, were all shifted to a common celestial reference system using preliminary optical identifications. A PSPC

image with a pixel size of 5 arcsec, covering the most sensitive area of the field of view (FOV), with a radius of ~ 20 arcmin, has been accumulated in the standard PSPC “hard” energy band 0.5–2 keV (pulseheight channel 52–201). This choice optimizes the angular resolution of the PSPC and the signal to noise ratio for the detection of faint extragalactic sources. It is also relatively insensitive to neutral hydrogen absorption column densities below $\sim 10^{21} \text{ cm}^{-2}$. For the calculation of hardness ratios we additionally analysed the PSPC data in the “soft” band and further subdivided the hard band into two: H1 and H2. Details about the energy bands are given in Table 2. Fig. 1a shows a contour plot of the PSPC image in the hard band.

The same area has also been covered by a set of raster scan observations with the ROSAT HRI (David et al., 1996). A total of ~ 100 pointings of roughly 2 ksec exposure each, has been placed on a regular grid with a step size of ~ 2 arcmin. The HRI FOV has a size of roughly 36×36 arcmin. The inner, most sensitive part of the field, where the off-axis blur of the telescope can be neglected, has a radius of roughly 8 arcmin. The raster scan step size is much smaller than the HRI FOV, thus the resulting exposure covers the survey area smoothly, with a rather homogeneous point spread function (PSF) across the field. The total exposure time accumulated for the raster scan is 205.50 ksec, comparable to the PSPC pointing. The individual HRI pointing data provided by the ROSAT Standard Analysis System SASS (Voges 1992) have been merged into a single mosaïque, after separate astrometrical solutions have been applied to each dataset, in order to correct for residual boresight and scale factor errors in the HRI data (see below). The HRI raster image has been accumulated in the restricted pulseheight channel range 1–9, which significantly reduces the detector background with a minimum loss ($\sim 7\%$) of cosmic X-ray photons (David et al., 1996). Using this channel selection, the HRI is sensitive to cosmic X-ray photons in the full ROSAT energy range 0.1–2.4 keV. Fig. 1b shows the resulting HRI raster scan image on the same scale as the PSPC data.

From Fig. 1 it is obvious, that the HRI raster scan, although having significantly higher resolution, is not nearly as sensitive as the PSPC observation which, however, is reaching the confusion limit (see below). In an attempt to reach an unconfused sensitivity limit comparable or deeper than the PSPC exposure, at least in a substantial fraction of the PSPC FOV, we performed an ultradeep HRI exposure of 1 Msec in a single pointing direction. The ROSAT attitude system shows residual pointing errors on the order of several arcsec, which can lead to a corresponding positional shift of the resulting image (see below). Uncorrected aspect errors can also lead to a substantial ellipticity of the HRI images of point sources (David et al., 1996), thus reducing resolution and sensitivity. To some degree these aspect errors can be corrected for, if one or

Table 1. Observation Summary

Start Date	End Date	Instrument	Exp. [s]
1990 Apr 16	1991 May 21	PSPC	67989
1991 Apr 25	1991 May 5	HRI raster	86778
1991 Oct 25	1991 Nov 2	PSPC	24327
1991 Oct 27	1991 Nov 9	HRI raster	116635
1992 Apr 15	1992 Apr 24	PSPC	66272
1992 Apr 18	1992 Apr 18	HRI raster	2082
1992 Nov 29	1992 Nov 29	PSPC	2082
1993 Apr 26	1993 May 9	PSPC	46740
1994 Oct 21	1994 Nov 7	HRI	106565
1995 Apr 15	1995 May 11	HRI	294483
1995 Oct 26	1995 Nov 27	HRI	200358
1996 May 1	1996 May 29	HRI	319590
1997 Apr 15	1997 Apr 28	HRI	191094

more bright optically identified X-ray sources are present in the image. In order to allow this procedure, we selected a pointing direction for the ultradeep HRI exposure, which is inside the PSPC field of view, but shifted about 10 arcmin to the North-East of the PSPC center, this way covering a region containing about 10 relatively bright X-ray sources known from the PSPC and the HRI raster scan. The ultradeep HRI exposure is centered at the direction $RA(2000) = 10^h 52^m 43^s$, $DEC(2000) = 57^\circ 28' 48''$. In some situations the automatic ROSAT HRI standard analysis system is too conservative in rejecting time intervals with supposedly high background. In particular using the background-optimized HRI channel range 1-9, we found an optimum point-source detection sensitivity including all exposure intervals with good attitude data. For the ultradeep survey we therefore selected events using a custom made procedure after having joined the SASS accepted and rejected event files. This resulted in a net observing time of 1112.09 ksec, a gain of $\sim 20\%$ compared to the SASS products. The individual datasets obtained in different semesters were shifted to the same reference system as the PSPC data, using preliminary optical identifications. The HRI image in the pulseheight channel range 1-9 is shown in Fig. 1c on the same scale as the PSPC image, which makes the shift to the North-East quite apparent.

3. Detection algorithm

The images in Fig. 1 have been analysed using an improved version of the interactive analysis system EXSAS (Zimmermann et al. 1994). The first steps of the detection procedure, i.e. the local detect algorithm LDETECT, the bicubic spline fit to the background map and the map detection algorithm MDETECT have been described in H93. The detection threshold of these algorithms has been set at a very low likelihood value so that the resulting list of possible source positions contains several hundred spurious detections. This position list has then been fed

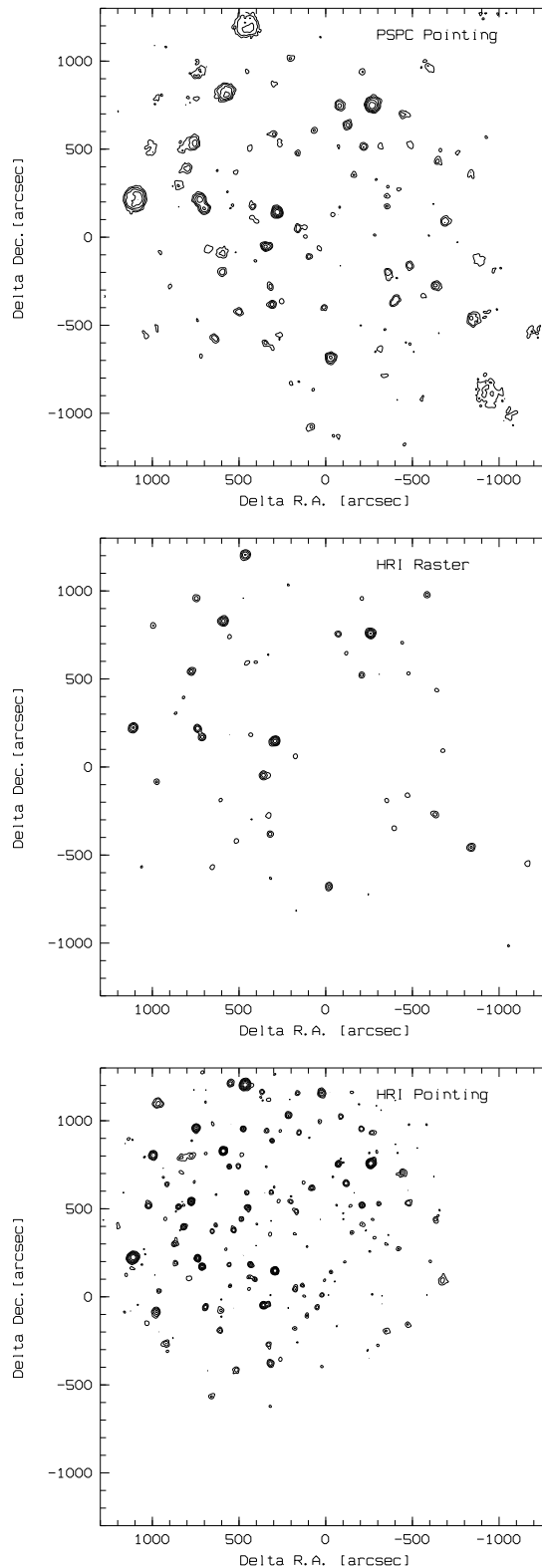


Fig. 1. ROSAT Deep Survey images in the Lockman Hole: (a) PSPC 207 ksec pointing, (b) HRI 205 ksec raster scan and (c) HRI 1112 ksec pointing. The images are all centered at the PSPC pointing direction (see text).

into the “multi-ML” crowded field detection and parameter estimation algorithm first described by Hasinger et al. (1994a). This method, which has been implemented into EXSAS, works on binned image data and fits superpositions of several PSF profiles on top of an external background to sections of the data (typically sub-images of arcmin size). Best-fit positions and normalizations are obtained by maximizing the likelihood statistic \mathcal{L} (Cash 1979) or, correspondingly, by minimizing the quantity

$$\mathcal{S} = -2\ln\mathcal{L} = -2 \sum_{i,j} (Y_{mod}(i,j) - N(i,j)\ln Y_{mod}(i,j)) \quad (1)$$

$Y_{mod}(i,j)$ is the sum of all model point source contributions plus the background value in the image pixel $[i,j]$ and N is the measured number of photons in pixel $[i,j]$. For ROSAT PSPC and HRI data the multi-component PSF (Hasinger et al., 1994b; David et al., 1996) is approximated by a single Gaussian function with a width increasing with off-axis angle. The significance $\Delta\mathcal{S}$ of any of the individual point source contributions is then estimated by a likelihood ratio test between the best fit with and without the corresponding component. If $\Delta\mathcal{S}$ falls below a threshold value, the corresponding component is omitted from the next iteration and only significant components are maintained. Since $\Delta\mathcal{S}$ follows a χ^2 distribution, the errors of the best-fit parameters (68% confidence single parameter of interest) are determined by searching the parameter space for which $\Delta\mathcal{S} = \mathcal{S} - \mathcal{S}_{min} = 1$. Before the next region of interest is fit, the current PSF contributions are added to the background model.

The complete source detection and parameter estimation procedure is too complicated to validate its results and e.g. quantify its detection efficiency analytically. We therefore performed extensive simulations of artificial ROSAT fields run through the same set of algorithms to study their properties (see below). Based on these simulations we have chosen a likelihood detection threshold of $\Delta\mathcal{S} = 16$, corresponding to a 4σ detection. Formally, the probability of a spurious detection with such a threshold is 6×10^{-5} per resolution element, which would correspond to less than one spurious detection per field of view. We will see in Sect. 6 that in practice the effective detection limit is set by source confusion. Observed fluxes in the 0.5–2 keV band are calculated for each source using the detected counts, the corresponding exposure time and vignetting correction, an energy-to-flux conversion factor (ECF) and a PSF-loss correction factor (PCF) determined from simulations (see below). In order to derive the ECF we assumed a power law spectrum with photon index 2 and galactic absorption, folded through the instrument response. Table 2 gives a summary of the various energy bands and correction factors for different detectors. For the PSPC hard band, because of the restricted energy range, the ECF is almost insensitive to N_H and to the assumed spectral shape for a wide range of absorptions and

spectral indices. On the contrary, the HRI is very sensitive to absorption and spectral shape because of its lack of energy resolution. Unabsorbed sources with steep spectra are favoured by the HRI.

Table 2. Energy bands and correction factors

Detector	Band	Energy [keV]	Pulseheight Channels	ECF ^a	PCF ^b
PSPC	H	0.5-2.0	52-201	0.836	0.90
PSPC	S	0.1-0.4	11-41	1.519	0.90
PSPC	H1	0.5-0.9	52-90	0.349	0.90
PSPC	H2	0.9-2.0	91-201	0.487	0.90
HRI		0.1-2.4	1-9	0.586	0.92

^a Energy to counts conversion factor in *cts/s* for a source with 0.5–2 keV flux $10^{-11} \text{ erg cm}^{-2} \text{ s}^{-1}$

^b PSF loss correction factor from simulations

For the calculation of hardness ratios, PSPC images were also analysed in the soft (S) and the split hard (H1, H2) bands (see Table 2), however with fixed positions. The standard ROSAT soft and hard hardness ratios HR1 and HR2 have been used.

$$HR1 = \frac{H - S}{H + S} \quad HR2 = \frac{H2 - H1}{H2 + H1} \quad (2)$$

4. Astrometric corrections

The ROSAT SASS performs various corrections to the individual PSPC and HRI photons, including detector linearisation, optical distortion, boresight and attitude correction. The large set of X-ray sources with reliable optical identifications in the Lockman Hole allows for the first time to check and crosscalibrate with high accuracy the ROSAT astrometry with absolute celestial positions.

A complete sample of X-ray sources in the Lockman Hole with fluxes down to $5.5 \times 10^{-15} \text{ erg cm}^{-2} \text{ s}^{-1}$ has been optically identified (Schmidt et al., 1997, paper II). The positions of the optical counterparts have been derived from Palomar 200” CCD drift scans and have an absolute accuracy of ~ 0.5 arcsec. Using the set of point-like X-ray sources optically identified with AGN and stars, we could derive astrometrical solutions for the PSPC and HRI data, respectively. For the deep PSPC and HRI pointing observations astrometrical solutions were fit to the deviation between X-ray and optical positions. The transformations contained the following parameters: $\Delta(RA)$ and $\Delta(DEC)$ position shifts, $\Delta(\Phi)$ roll angle and $F(Sc)$ scale factor correction. The best-fit parameters were determined by a χ^2 -fit, using the individual statistical position errors of the X-ray sources and assuming an error of 0.5” for the optical positions. In order to take account

Table 3. Astrometric solutions

Instrument	Nr. IDs	E_{sys} ["]	χ^2	$F(Sc)$	$\Delta(\Phi)$ [']	$\Delta(RA)$ ["]	$\Delta(DEC)$ ["]
PSPC Pointing	47	3.0	1.28	1.0020 ± 0.0007	-2.9 ± 2.0	-0.2 ± 0.5	-0.1 ± 0.5
HRI Pointing	32	0.5	1.05	0.9972 ± 0.0006	1.2 ± 1.4	-0.1 ± 0.3	0.3 ± 0.3
HRI Raster	31	0.5	1.07	1.0004 ± 0.0006	1.0 ± 1.5	-0.3 ± 0.4	-0.3 ± 0.4
Combined	43	0.0	1.36	1.0001 ± 0.0003	-1.1 ± 0.7	-0.1 ± 0.2	0.0 ± 0.2

of possible additional deviations in the X-ray positions, which may result from residuals in the detector linearization or from X-ray source confusion, we added in quadrature a constant systematic position error E_{sys} to the statistical error for each source. The size of this additional error (see column 3 of Table 3) was chosen such that the reduced χ^2 approached a value of 1.

Table 3 shows the result of the astrometric solutions. As expected, the residual position shifts are all negligible, because all data have been shifted to a common system before. The roll angle correction applied by the SASS is already very good; the roll angle corrections $\Delta(\Phi)$ in our deep datasets are all smaller than a few arcmin. The only significant astrometrical correction which is necessary for both PSPC and HRI is a scale factor correction of order 0.2–0.3%. For the PSPC this correction factor is marginally significant and can probably be neglected for most datasets. For the HRI the scale factor error is consistent with the estimate derived from HRI data of M31 (David et al., 1996), but our data is more accurate and provide the first significant measurement of this quantity. The HRI scale factor error corresponds to a position deviation of about 4 arcsec across the HRI FOV and needs to be taken into account to achieve highest astrometrical accuracy. The residual systematic position errors across the HRI FOV are very small (0.5"), while the PSPC has residual systematic errors of order 3", most likely because of source confusion and the broader PSF (see below).

For the HRI raster scan data, every individual short pointing was first shifted to a common celestial reference system and corrected for the above scale factor error, before all photons were merged to one dataset. As a test we applied the same astrometrical transformation fit as to the pointed observations. The fact that all fit parameters are consistent with their expected values and that the required residual systematic errors are of the same order as for the individual HRI pointing shows that the shift- and merge procedure was successful. Finally, the last row in Table 3 shows an astrometric fit to the X-ray source catalogue combined from all three datasets (see below). As expected, all astrometric parameters are consistent with their expected values. The reduced χ^2 of the combined fit is acceptable without the addition of extra systematic errors. The distribution of positional errors for uniquely

identified sources is therefore as expected, thus validating the calculation of the positions and errors.

5. X-ray source catalogue

The scale factor corrections determined in the previous section were applied to the three individual detection lists from PSPC pointing, HRI pointing and HRI raster scan observation and the corresponding systematic position errors were added in quadrature to the statistical errors determined in the multi-ML detection procedure. Finally, the three individual position lists were merged into a single source list. For all detections, which were positionally coincident within their 90% error radii, weighted average positions and position errors were calculated. These form the basis for the final X-ray source catalogue, presented in Table 4. This catalogue contains all objects with PSPC fluxes higher than $1.11 \times 10^{-14} \text{ erg cm}^{-2} \text{ s}^{-1}$ at off-axis angles smaller than 18.5 arcmin and all objects with fluxes larger than $0.56 \times 10^{-14} \text{ erg cm}^{-2} \text{ s}^{-1}$ inside an off-axis angle of 12.5 arcmin.

Column (1) of Table 4 gives the official ROSAT name, column (2) an internal source number. Columns (3) and (4) give the weighted average coordinates of the X-ray sources for an equinox of J2000.0. Column (5) shows the 1σ position error of the source, including statistical and systematic errors. A capital P, H, or R after the position error indicates, whether the dominant weight to the X-ray position comes from the PSPC pointing, HRI pointing or HRI raster scan, respectively. Column 6 gives the 0.5–2 keV flux of the source in units of $10^{-14} \text{ erg cm}^{-2} \text{ s}^{-1}$, derived from the ROSAT PSPC hard band and its 1σ error. Column (7) and (8) give the soft and hard hardness ratios defined above.

6. Verification of the analysis procedure by simulations

The ROSAT deep survey exposures are probing the limits of observational and data analysis procedures. In order to obtain a reliable and quantitative characterization and calibration of the source detection procedure, detailed simulations of large numbers of artificial fields, analysed through exactly the same detection and param-

Table 4. Source Catalogue

Source Name	Nr.	R.A. (2000)	Dec. (2000)	Err. [$^{\circ}$]	f_x	HR1	HR2
RX J105421.1+572545	28	10 54 21.1	57 25 44.5	1.0H	19.90 ± 0.41	1.00 ± 0.06	-0.27 ± 0.02
RX J105131.1+573440	8	10 51 31.1	57 34 40.4	0.8H	11.84 ± 0.33	-0.24 ± 0.02	-0.47 ± 0.02
RX J105316.8+573552	6	10 53 16.8	57 35 52.4	0.9H	8.82 ± 0.33	-0.29 ± 0.02	-0.40 ± 0.02
RX J105239.7+572432	32	10 52 39.7	57 24 31.7	0.8H	6.50 ± 0.30	-0.55 ± 0.02	-0.16 ± 0.03
RX J105335.1+572542	29	10 53 35.1	57 25 42.4	0.8H	5.13 ± 0.25	-0.34 ± 0.03	-0.36 ± 0.03
RX J105331.8+572454	31	10 53 31.8	57 24 53.9	0.9H	3.57 ± 0.18	-0.18 ± 0.04	-0.40 ± 0.03
RX J105339.7+573105	16	10 53 39.7	57 31 5.3	0.9H	3.56 ± 0.18	-0.59 ± 0.02	-0.43 ± 0.03
RX J105020.2+571423	56	10 50 20.2	57 14 22.8	1.8R	3.52 ± 0.17	-0.44 ± 0.02	-0.37 ± 0.04
RX J105201.5+571044	62	10 52 1.5	57 10 44.2	1.6R	3.20 ± 0.18	-0.31 ± 0.03	-0.50 ± 0.03
RX J105247.9+572116	37	10 52 47.9	57 21 16.3	0.8H	2.54 ± 0.13	-0.73 ± 0.02	-0.19 ± 0.06
RX J105410.3+573039	20	10 54 10.3	57 30 39.3	1.4H	2.43 ± 0.18	0.47 ± 0.11	-0.19 ± 0.06
RX J105154.4+573438	9	10 51 54.4	57 34 38.0	1.0H	1.88 ± 0.15	-0.23 ± 0.06	-0.18 ± 0.06
RX J105318.1+572042	41	10 53 18.1	57 20 42.0	2.4H	1.87 ± 0.13	0.03 ± 0.10	-0.46 ± 0.06
RX J105344.9+572841	25	10 53 44.9	57 28 40.5	1.1H	1.84 ± 0.15	-0.09 ± 0.07	0.13 ± 0.09
RX J105015.6+572000	42	10 50 15.6	57 20 0.2	4.7P	1.69 ± 0.15	-0.36 ± 0.06	-0.14 ± 0.07
RX J105046.1+571733	48	10 50 46.1	57 17 32.8	1.8R	1.64 ± 0.17	-0.08 ± 0.08	-0.00 ± 0.07
RX J105149.0+573249	12	10 51 49.0	57 32 48.6	1.0H	1.57 ± 0.14	1.00 ± 0.78	0.28 ± 0.08
RX J105324.6+571236	59	10 53 24.6	57 12 35.7	2.8P	1.50 ± 0.13	0.27 ± 0.14	-0.20 ± 0.07
RX J105039.7+572335	35	10 50 39.7	57 23 35.1	1.8R	1.48 ± 0.15	-0.29 ± 0.06	-0.19 ± 0.06
RX J105348.7+573033	117	10 53 48.7	57 30 33.5	1.4H	1.46 ± 0.18	1.00 ± 1.51	0.19 ± 0.10
RX J105350.3+572710	27	10 53 50.3	57 27 9.6	2.0H	1.39 ± 0.08	0.16 ± 0.17	0.18 ± 0.07
RX J105008.2+573135	73	10 50 8.2	57 31 34.7	8.2P	1.39 ± 0.13	0.78 ± 0.51	0.57 ± 0.44
RX J105243.1+571544	52	10 52 43.1	57 15 44.4	1.2H	1.32 ± 0.12	-0.36 ± 0.06	0.00 ± 0.08
RX J105108.4+573345	11	10 51 8.4	57 33 45.4	1.6H	1.27 ± 0.12	0.18 ± 0.12	0.32 ± 0.11
RX J105055.3+570652	67	10 50 55.3	57 6 51.9	8.1P	1.24 ± 0.15	0.23 ± 0.16	0.01 ± 0.11
RX J105020.3+572808	26	10 50 20.3	57 28 7.8	6.5P	1.20 ± 0.11	-0.06 ± 0.14	0.13 ± 0.11
RX J105009.3+571443	55	10 50 9.3	57 14 42.8	6.6P	1.17 ± 0.15	0.02 ± 0.06	0.13 ± 0.11
RX J105230.3+573914	2	10 52 30.3	57 39 13.8	1.3H	1.16 ± 0.14	-0.03 ± 0.17	0.01 ± 0.11
RX J105307.2+571506	54	10 53 7.2	57 15 5.6	1.9H	1.12 ± 0.14	0.05 ± 0.10	0.04 ± 0.09
RX J105319.0+571852	45	10 53 19.0	57 18 51.9	1.5H	1.04 ± 0.14	0.02 ± 0.12	-0.03 ± 0.08
RX J105137.4+573044	19	10 51 37.4	57 30 44.4	1.0H	0.99 ± 0.11	-0.24 ± 0.07	-0.18 ± 0.09
RX J105114.5+571616	504	10 51 14.5	57 16 16.0	1.8R	0.96 ± 0.12	-0.38 ± 0.07	-0.12 ± 0.09
RX J105105.2+571924	43	10 51 5.2	57 19 23.9	1.9R	0.94 ± 0.09	-0.28 ± 0.07	-0.03 ± 0.10
RX J105225.1+572304	36	10 52 25.1	57 23 3.7	1.8R	0.92 ± 0.08	0.05 ± 0.19	0.08 ± 0.11
RX J105120.2+571849	46	10 51 20.2	57 18 49.2	1.9R	0.89 ± 0.09	-0.18 ± 0.09	-0.13 ± 0.08
RX J105127.0+571129	61	10 51 27.0	57 11 29.0	6.0P	0.79 ± 0.09	-0.07 ± 0.14	-0.27 ± 0.13
RX J105329.2+572104	38	10 53 29.2	57 21 3.7	1.3H	0.78 ± 0.11	-0.30 ± 0.08	-0.53 ± 0.07
RX J105248.4+571203	60	10 52 48.4	57 12 2.7	5.0P	0.78 ± 0.10	-0.00 ± 0.19	-0.38 ± 0.09
RX J105242.5+573159	14	10 52 42.5	57 31 59.2	1.3H	0.72 ± 0.09	0.72 ± 0.52	0.44 ± 0.15
RX J105244.4+571732	47	10 52 44.4	57 17 31.9	1.6H	0.71 ± 0.09	-0.35 ± 0.08	-0.28 ± 0.10
RX J105257.1+572507	30	10 52 57.1	57 25 7.2	0.9H	0.70 ± 0.09	-0.53 ± 0.05	-0.47 ± 0.07
RX J105117.0+571554	51	10 51 17.0	57 15 54.1	5.1P	0.66 ± 0.11	0.04 ± 0.22	-0.10 ± 0.14
RX J105104.2+573054	17	10 51 4.2	57 30 53.7	1.6H	0.62 ± 0.10	0.11 ± 0.19	-0.14 ± 0.14
RX J105244.7+572122	814	10 52 44.7	57 21 22.2	1.3H	0.61 ± 0.16	0.68 ± 0.68	0.51 ± 0.18
RX J105217.0+572017	84	10 52 17.0	57 20 17.1	2.0H	0.60 ± 0.08	0.68 ± 0.71	0.85 ± 0.32
RX J105259.2+573031	77	10 52 59.2	57 30 30.8	1.1H	0.59 ± 0.10	-0.14 ± 0.13	-0.16 ± 0.14
RX J105206.0+571529	53	10 52 6.0	57 15 28.7	4.6P	0.58 ± 0.07	-0.15 ± 0.12	0.82 ± 0.17
RX J105237.7+573107	116	10 52 37.7	57 31 6.5	5.1P	0.57 ± 0.10	1.00 ± 0.84	-0.48 ± 0.09
RX J105224.7+573010	23	10 52 24.7	57 30 10.2	1.5H	0.56 ± 0.07	0.02 ± 0.20	-0.41 ± 0.10
RX J105237.9+571254	58	10 52 37.9	57 12 53.5	6.2P	0.56 ± 0.08	0.07 ± 0.21	-0.42 ± 0.09

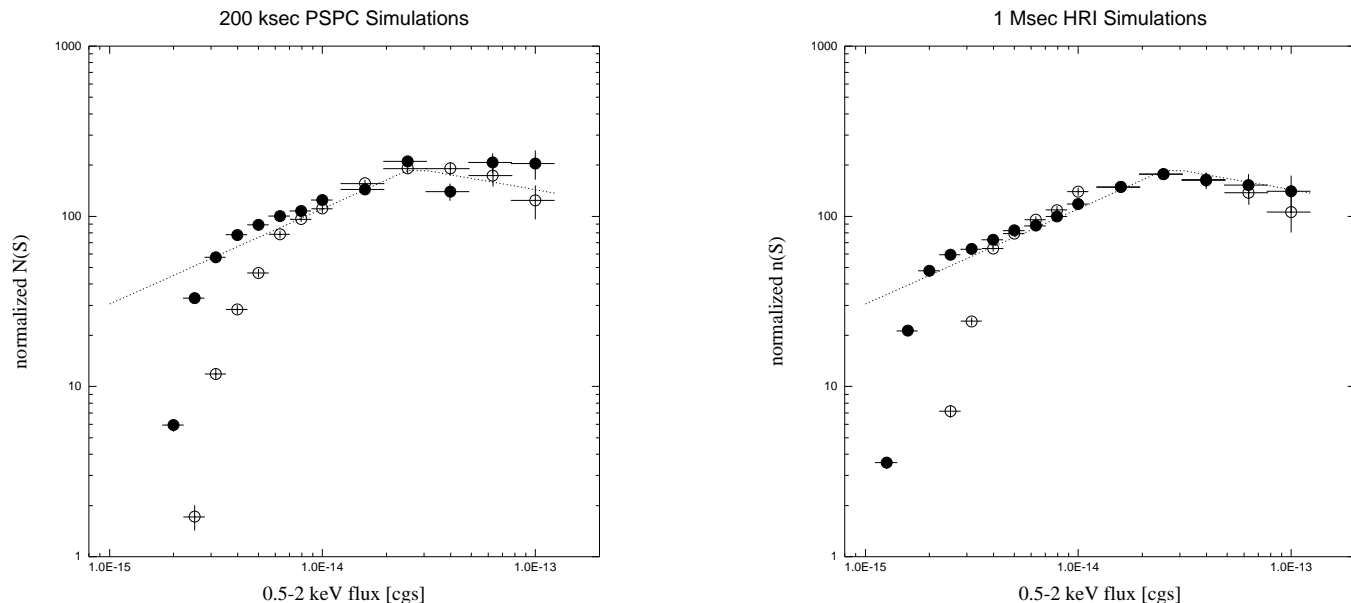


Fig. 2. Comparison of detected $\log(N)$ – $\log(S)$ relation to input source counts in the 0.5–2 keV band. The dotted line shows the differential source counts $n(S)$ input to the simulations, normalized to a Euclidean slope (see equation 3 and 4). The filled and open circles show the detected differential $\log(N)$ – $\log(S)$, derived from (a) 66 simulated PSPC fields of 200 ksec exposure, and (b) 100 simulated HRI fields of 1 Msec exposure each. Filled symbols correspond to sources at off-axis angles smaller than 12.5 arcmin for the PSPC and 10 arcmin for the HRI, respectively. Open symbols refer to larger off-axis angles.

eter estimation procedure as the real data, are required. The simulations in H93 demonstrated that source confusion sets the ultimate limit in ROSAT deep survey work with the PSPC. The crowded-field multi-ML detection algorithm used in the current paper was specifically designed to better cope with source confusion. Therefore we felt it necessary to calibrate its efficiency and verify its accuracy through new simulations. We have simulated sets of PSPC and HRI observations with 200 ksec and 1Msec exposure, respectively, approximating our current observation times. In order to compare our results with those of shallower PSPC surveys in the literature we simulated additional sets of observations of 50 and 110 ksec each. The soft X-ray $\log(N)$ – $\log(S)$ function (0.5–2 keV) has been simulated according to the ROSAT deep survey findings (H93) as a broken power law function for the differential source counts (all fluxes are given in units of $10^{-14} \text{ erg cm}^{-2} \text{ s}^{-1}$):

$$\begin{aligned} n(S) &= n_1 \times S^{-b_1} \text{ for } S > S_b, \quad n_1 = 238.1 \quad b_1 = 2.72 \\ &= n_2 \times S^{-b_2} \text{ for } S < S_b, \quad n_2 = 111.0 \quad b_2 = 1.94 \quad (3) \\ S_b &= 2.66 \end{aligned}$$

As shown in H93, the final results are relatively independent from the actual $\log(N)$ – $\log(S)$ parameters chosen for the artificial fields. In the simulations point sources are placed at random within the FOV, with fluxes drawn at random from the $\log(N)$ – $\log(S)$ function down to a minimum source flux of 4.65×10^{-18} , where formally all the X-

ray background is resolved for the assumed source counts. (For the later comparison between input and output catalogues only input sources with fluxes larger than 10^{-16} or more than 5 simulated photons are maintained in the input catalogue.) For each source the ROSAT vignetting correction, the corresponding ECF (see Table 2) and the exposure time (50, 110, 200 ksec for PSPC, 1Msec for HRI) are applied to the source flux to obtain the expected number of source counts. The actual source counts are drawn from a Poissonian distribution and folded through the point spread function. The realistic multi-component point spread function model is taken from Hasinger et al. (1994b) for the PSPC and from David et al. (1996) for the HRI. Finally, all events missing in the field, i.e. particle background, non-source diffuse background and photons not simulated in the $\log(N)$ – $\log(S)$ function are added as a smooth distribution to the image.

A total of 66 PSPC fields of an exposure of 200 ksec, 50 fields of 50 ksec and 27 fields of 110 ksec each has been simulated in the 0.5–2 keV band. The corresponding number of HRI fields with 1 Msec exposure was 100. All simulated exposures have been analysed through exactly the same sequence of detection, background estimation and parameter estimation algorithms as the real data. The 200 ksec PSPC images were analysed in two ranges of off-axis angles: 0–12.5 arcmin and 12.5–18.5 arcmin, the HRI 1Msec images for off-axis angle ranges of 0–10 arcmin and 10–15 arcmin and the 50 and 110 ksec PSPC exposures inside 15 arcmin.

6.1. Flux conservation

For each detected source the process of “source identification” has been approximated by a simple positional coincidence check. A detected source was identified with the counterpart from the input list, which appeared closest to the X-ray position within a radius of 30 arcsec. A direct comparison between the detected and simulated number of photons for sources with fluxes brighter than 5×10^{-14} cgs shows, that the scale of the output flux is the same as that of the input flux to an accuracy of better than 1%. This means that at bright fluxes no systematic errors exist, apart from the PSF loss factor of 0.90 (see Table 2), which is corrected for globally in the simulations as well as in the real data. This correction is necessary, probably due to the misfit between the broader components of the real PSF and the simple Gaussian model in the multi-ML fit. For the HRI this PSF loss factor is 0.92 (see Table 2).

6.2. Limiting sensitivity and $\log(N)$ – $\log(S)$ relation

A $\log(N)$ – $\log(S)$ function has been derived for the simulated detected sources (in rings of 0–12.5 arcmin and 12.5–18.5 arcmin for the PSPC and rings of 0–10 arcmin and 10–15 arcmin, respectively for the HRI). For easier comparison the differential source counts $n(S)$ were divided by the source counts expected for a Euclidean distribution, i.e.:

$$n(S)_{cor} = n(S) \times S^{2.5} \quad (4)$$

Fig. 2 shows the comparison between the input $\log(N)$ – $\log(S)$ and the detected number counts in this representation for both 200 ksec PSPC and the 1 Msec HRI simulations. The faintest sources detected in the PSPC at small off-axis angles have a flux of 2×10^{-15} cgs. For a flux lower than 3×10^{-15} cgs, the source counts fall significantly below the simulated $\log(N)$ – $\log(S)$ function, while above this flux there is a slight excess. These effects are well known from ROSAT PSPC deep survey simulations and are due to a number of selection and confusion effects. At larger off-axis angles the sensitivity is reduced correspondingly. The faintest HRI sources reach down to fluxes of 10^{-15} cgs and the deviation between input and output source counts becomes insignificant above a flux of 1.8×10^{-15} cgs for small off-axis angles. Again, at larger angles the sensitivity is reduced. The source confusion effects are much less pronounced in the HRI.

The deviation between input- and output source counts in the simulations can be used to correct the observed $\log(N)$ – $\log(S)$ function down to the faintest limiting fluxes (see H93). Utilizing all sources detected in the real PSPC and HRI pointing observations inside off-axis angles of 18.5 and 15 arcmin, respectively, we calculated the corrected observed $\log(N)$ – $\log(S)$ function displayed in Fig. 3. The new PSPC data agree very well with the source

counts published earlier and extend those down to a flux of 2×10^{-15} cgs and a surface density of 640 ± 75 deg $^{-2}$. The HRI $\log(N)$ – $\log(S)$ function for the first time extends the source counts down to fluxes of 10^{-15} cgs and reaches a surface density of 970 ± 150 deg $^{-2}$, about a factor of two higher than any previous X-ray determination of source counts. All data are consistent with the previous determination of source counts and fluctuation limits (H93).

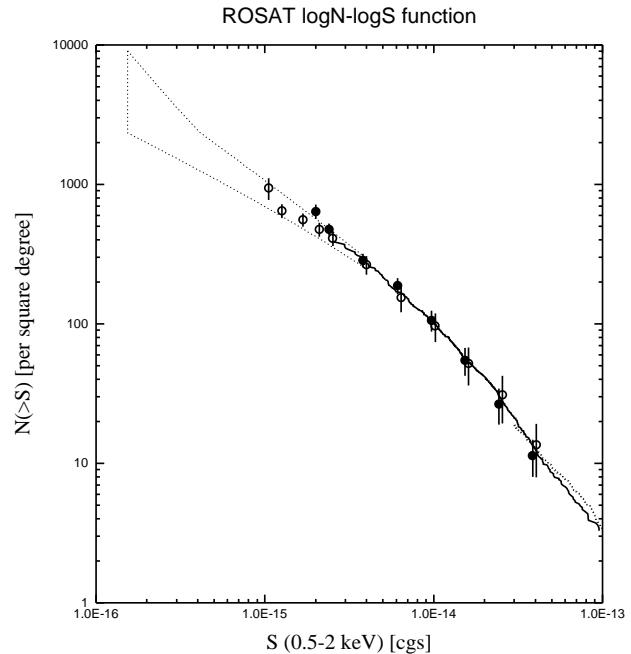


Fig. 3. Measured ROSAT $\log(N)$ – $\log(S)$ function in the Lockman Hole. Filled circles give the source counts from the 207 ksec PSPC observation. Open circles are from the ultradeep HRI observation (1112 ksec), slightly shifted in flux in order to avoid overlap of error bars. The data are plotted on top of the source counts (solid line) and fluctuation limits (dotted area) from Hasinger et al. (1993). The dotted line at bright fluxes refers to the total source counts in the RIXOS survey (Mason et al., 1996, priv. comm.).

6.3. Source confusion

The detected source catalogues are affected by biases and selection effects present in the source-detection procedure. The most famous of those is the Eddington bias, which produces a net gain of the number of sources detected above a given flux limit as a consequence of statistical errors in the measured flux (see discussion in H93). Another selection effect, most important in the deep fields considered here, is source confusion. The net effect of source confusion is difficult to quantify analytically, because it can affect the derived source catalogue in different ways:

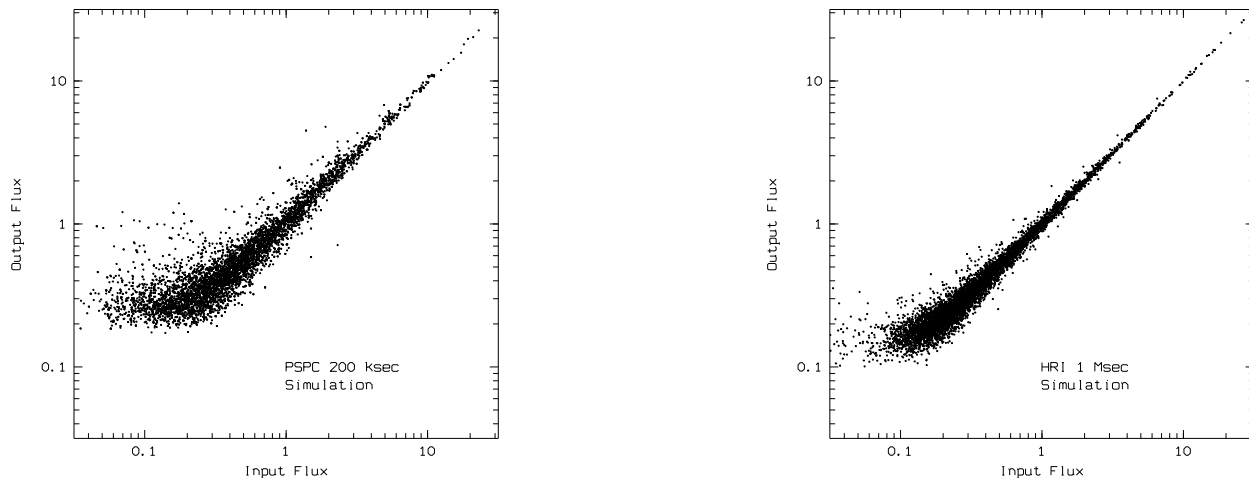


Fig. 4. Detected flux versus input flux for (a) 66 simulated PSPC fields of 200 ksec exposure, and (b) 100 simulated HRI fields of 1 Msec exposure each. The PSPC data is for off-axis angles smaller than 12.5 arcmin, for the HRI the limit is 10 arcmin. Fluxes are in units of $10^{-14} \text{ erg cm}^{-2} \text{ s}^{-1}$.

(1) two sub-threshold sources could be present in the same resolution element and thus mimic a single detected source. This leads to a net gain in the number of sources, similar to the Eddington bias.

(2) two sources above the threshold could merge into a single brighter source. In this case one source is lost and one is detected at a higher flux. Whether the total flux is conserved or not depends on the distance between the two sources and on the details of the source detection algorithm.

(3) the detection algorithm cannot discriminate close sources with very different brightness, which results in a net loss of fainter sources.

The effects of confusion become immediately obvious in fig 4 where for each detected source the detected flux is compared to the flux of the nearest input source within $30''$. While for bright sources there is an almost perfect match, there is a significant systematic deviation for fainter X-ray sources, where most objects appear at fluxes significantly brighter than their input counterparts, which is a direct indication of confusion because every detected source is only associated with one input source while its flux may be contributed from several sources.

We can quantify “confusion” e.g. by looking for sources, whose detected X-ray flux is significantly larger than their input flux. This means that a substantial fraction of the detected photons originates from other, contaminating sources. We define SR as the ratio of the de-

tected flux and the input flux increased by 3 times the statistical error:

$$SR = \frac{S_{det}}{S_{inp}} \cdot \frac{1}{1 + 3\sigma_S} \quad (5)$$

where σ_S is the fractional flux error. For practical purposes a flux ratio of $SR > 1.5$ has been chosen, above which significant position deviations might be expected. In Table 5, we give the *fraction of contaminated sources* FC with flux ratio SR larger than 1.5 as a function of detected flux for different surveys. Significant confusion (larger than 10%) sets in below a flux of $5 \times 10^{-15} \text{ cgs}$ for the 200 ksec PSPC observation and below 10^{-14} cgs for the 50 ksec observation. In contrast, the HRI confusion is negligible over almost the complete range of detected fluxes.

6.4. Effect of source confusion on optical identification

While it is obviously possible to correct for confusion effects on the source counts in a statistical way, the optical identification process relies on the position of individual sources. An independent measure of confusion is the fraction of sources with significant positional deviation from their respective counterparts. Fig. 5 shows for each simulated source the distance to the nearest source as a function of simulated input flux. As expected, bright sources have relatively small positional errors and therefore small deviations of a few arcsec between simulated and output position. For fainter sources there is an incompleteness limit. More and more input sources are not

Table 5. Confusion estimates^a

Flux range ^b [10 ⁻¹⁴ cgs]	200 ksec PSPC 0–12.5'			200 ksec PSPC 12.5–18.5'			110ksec PSPC 0–15'			50 ksec PSPC 0–15'			1 Msec HRI 0–10'		
	FC	FL	FU	FC	FL	FU	FC	FL	FU	FC	FL	FU	FC	FL	FU
2-10	2	1	0	6	3	8	3	2	2	1	1	1	0	0	0
1-2	3	4	3	9	14	11	7	3	5	4	7	7	0	0	0
0.5-1	7	10	5	14	38	26	9	19	11	11	33	19	1	0	0
0.2-0.5	12	38	16	16	78	34	11	62	22	14	74	19	2	3	1
0.1-0.2	20	81	24										11	47	10

^a Fraction of confused sources in percent according to different confusion measures (see text): FC is the percentage of contaminated sources, having an output flux significantly larger than their input flux ($SR > 1.5$). FL is the percentage of lost sources, having no detected source within 15" from the input position. FU is the fraction of unidentifiable detected sources, having no input source within 15" from the detected position. ^b detected flux for FC and FU, input flux for FL

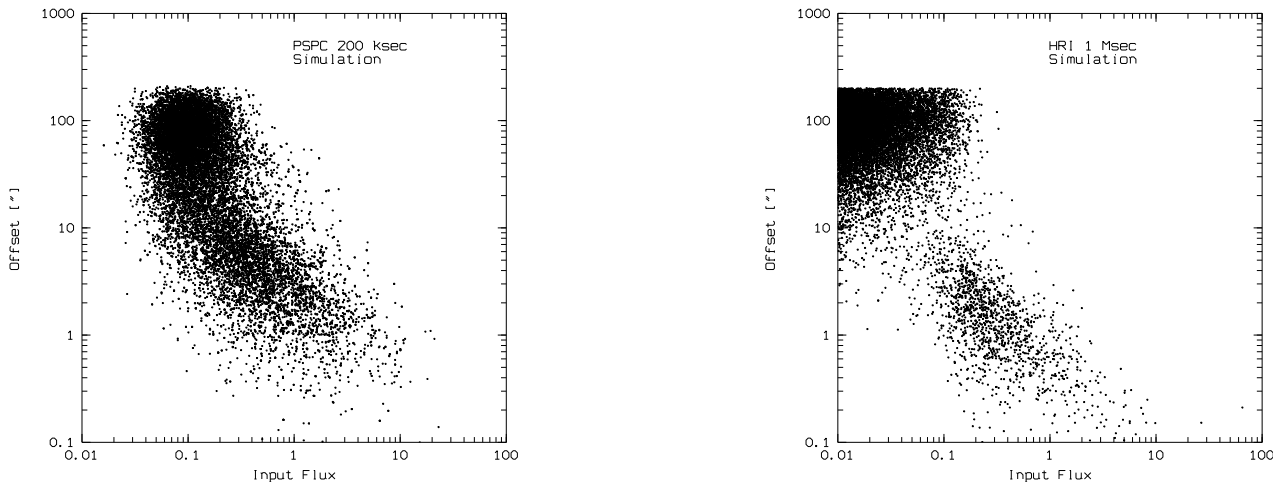


Fig. 5. Position deviation between input source and nearest output object as a function of input flux for the simulations in Fig. 2. The plot is cut off artificially for distances larger than 200 arcsec.

detected at all and therefore are matched to the nearest (but wrong) detected X-ray source. For the HRI simulation this yields a well-defined cloud of spuriously matched sources below a flux of $\sim 2 \times 10^{-15}$ cgs. For the PSPC this incompleteness limit sets in below $\sim 4 \times 10^{-15}$ cgs and the spurious match cloud is not disjunct of the detected source correlation track. Confusion leads to a halo of PSPC sources with significantly larger positional deviation than the bulk of detected sources at the same flux. A practical limiting radius for the optical identification of faint ROSAT X-ray sources is 15", which is used by several authors (see e.g. Bower et al., 1996, Georgantopoulos et al., 1996). In Table 5 we give the *fraction of lost sources* $FL(> 15")$ which have no detected source within a distance of 15" from the input position.

The quantity FL is a good tool to define a reliable flux limit for a survey, because it combines both the confusion and incompleteness effects. For practical applications we need, however, a quantity that can be applied to existing surveys, i.e. to detected sources. To do this, we invert the question that led to the quantity FL and ask: how many of the detected sources appear at a detected position further away from any "reasonable" input position than e.g. 15". For this purpose we exclude as reasonable input positions sources with input fluxes more than a factor 3 below the detected flux. This gives us an estimate of the *fraction of unidentifiable sources* in a survey, which we denote with the quantity FU.

The quantities FC, FL and FU are compared in Table 5 for different surveys and flux ranges. This table shows that, as expected, confusion effects increase dramatically

towards fainter fluxes. For fluxes above the incompleteness limit the different confusion measures, FC, FL and FU lead to similar estimates for the number of confused sources. Below this limit, FL increases dramatically, indicating severe incompleteness of the survey in addition to confusion. Using this table we have chosen the relatively conservative limits in flux and off-axis angles employed in the current survey, i.e. a flux limit of 5.5×10^{-15} for off-axis angles smaller than 12.5 arcmin and a flux limit of 1.1×10^{-14} for off-axis angles between 12.5 and 18.5 arcmin. In the discussion section we compare these simulations to shallower PSPC surveys in the literature.

7. Discussion

With a limiting flux of $\sim 10^{-15} \text{ erg cm}^{-2} \text{ s}^{-1}$, the X-ray survey in the *Lockman Hole* represents the deepest X-ray survey ever performed. The total observing time invested is quite comparable to that of other major astronomical projects, like e.g. the Hubble Deep Field (Williams et al., 1996). Because of the expected confusion in the PSPC it was clear from the beginning, that HRI data would be necessary to augment the PSPC identification process. Because of the smaller field-of-view of the HRI and because of its lower quantum efficiency, it was necessary to invest about a factor five more HRI time than PSPC time. Both the HRI raster scan, which provides excellent positions for all brighter objects in the PSPC field, and the HRI ultradeep survey in the (slightly offset) central part of the field allow almost complete optical identifications of sources down to $5.5 \times 10^{-15} \text{ erg cm}^{-2} \text{ s}^{-1}$ (see paper II). Apart from this, the ultradeep HRI data provides a survey in its own right, which is not yet fully exploited. It will ultimately lead to reliable optical identifications a factor of 3-4 deeper than the current survey. On the other hand, the Lockman Hole data are also of fundamental importance for other observations with the ROSAT HRI since they provided for the first time a significant determination of the HRI scale factor correction which is important for all high-quality astrometry with the HRI.

7.1. The ROSAT $\log(N)$ - $\log(S)$ function

The new PSPC and HRI data shown in Fig. 3 carry the resolved source counts a factor of 2.5 deeper than the most sensitive previous determinations (H93, Branduardi-Raymont et al., 1994). It is very reassuring to see that the source counts are still consistent with the previous fluctuation analyses (H93, Barcons et al., 1994). There are, however, some problems at the bright end of the source counts. In our previous paper we used the source counts from the EMSS (Gioia et al., 1990) to constrain the bright end ($S_{(0.5-2.0\text{keV})} > 1.8 \times 10^{-13}$) of the $\log(N)$ - $\log(S)$ relation. The first study to note a discrepancy between the EMSS and ROSAT counts was the RIXOS survey. Page et al. (1996) found, that the EMSS $\log(N)$ - $\log(S)$ for AGN is

significantly lower than the one from RIXOS. The source counts from the ROSAT All-Sky-Survey Bright Source Catalogue (Voges et al., 1996) confirm this trend and extend it to fluxes well above $10^{-12} \text{ erg cm}^{-2} \text{ s}^{-1}$ (Hasinger et al., 1997, in prep.). It appears that the $\log(N)$ - $\log(S)$ function at fluxes brighter than $10^{-13} \text{ erg cm}^{-2} \text{ s}^{-1}$ has a slope of $\beta_0 \sim 2.3$ and a normalization of ~ 91 and is therefore significantly flatter than what we assumed in H93 from a fit to the EMSS total source counts. The flatter $\log(N)$ - $\log(S)$ slope at bright fluxes has some consequences for the calculation of the resolved fraction.

7.2. The resolved fraction

As in H93 we restrict the analysis of the resolved fraction to the energy band 1-2 keV in order to minimize galactic contamination in the X-ray background spectrum. The absolute level and the spectrum of the X-ray background in this energy range is still a matter of debate (see the discussion in Hasinger 1996). In H93 we assumed a 1-2 keV background flux of $1.25 \times 10^{-8} \text{ erg cm}^{-2} \text{ s}^{-1} \text{ sr}^{-1}$. From ASCA data in the energy range 1-7 keV, Gendreau et al. (1995) have derived a flat spectrum with photon index 1.4 and a normalization of $8.9 \text{ keV cm}^{-2} \text{ s}^{-1} \text{ keV}^{-1}$ at 1 keV. Integrating this spectrum we derive a lower limit to the 1-2 keV XRB flux of $1.22 \times 10^{-8} \text{ erg cm}^{-2} \text{ s}^{-1} \text{ sr}^{-1}$. This can be contrasted to the earlier ROSAT PSPC determination of a steep spectrum in the 0.5-2 keV band, with photon index around 2 and a normalization around 13 (see Hasinger 1996). Integrating this over the 1-2 keV band yields a flux of $1.44 \times 10^{-8} \text{ erg cm}^{-2} \text{ s}^{-1} \text{ sr}^{-1}$, which is consistent with the background flux derived by Chen et al., 1997 from a joint ROSAT/ASCA fit (1.46 in the same units).

In H93 we integrated the analytic $\log(N)$ - $\log(S)$ function (Eq. 3) for fluxes brighter than $2.5 \times 10^{-15} \text{ erg cm}^{-2} \text{ s}^{-1}$, including a fit to the EMSS at fluxes brighter than $1.8 \times 10^{-13} \text{ erg cm}^{-2} \text{ s}^{-1}$. We obtained a resolved 1-2 keV flux of $0.74 \times 10^{-8} \text{ erg cm}^{-2} \text{ s}^{-1} \text{ sr}^{-1}$. If we follow the same prescription, but now integrating the H93 source counts above our limiting flux of $10^{-15} \text{ erg cm}^{-2} \text{ s}^{-1}$, we arrive at a resolved flux of 0.89 in the same units. If we, however, correct for the flatter slope of the bright end $\log(N)$ - $\log(S)$ (see above), we arrive at a resolved flux value of 0.99 (same units). We use this resolved flux in comparing with the total diffuse background in the 1-2 keV band.

If we adopt a 1-2 keV background flux of $1.45 \times 10^{-8} \text{ erg cm}^{-2} \text{ s}^{-1} \text{ sr}^{-1}$, we have resolved 68% of the 1-2 keV X-ray background at a flux of $10^{-15} \text{ erg cm}^{-2} \text{ s}^{-1}$. If, however, the lower ASCA spectrum with a flux of $1.22 \times 10^{-8} \text{ erg cm}^{-2} \text{ s}^{-1} \text{ sr}^{-1}$ holds, we have already resolved 81% of the background. We see, that the uncertainty in the resolved fraction is now dominated by the systematic error in the absolute background flux and not

Table 6. Comparison of ROSAT surveys

Survey ^a	Area ^b	T ^c	S_{lim}^d	Off ^e	Err ^f	S_{range}^g	FC ^h	FL ⁱ	FU ^j
RIXOS	~ 20	>8	3.0						
CRSS	3.9	>6	2.0						
DRS	1.4	21-49	0.3	15	15	0.3-0.6	13	62	23
MARA	0.2	55	0.5	15	15	0.5-1	11	33	19
NEP	0.2	79	1.0	15.5	15	1-2	6	6	7
UKDS	0.2	110	0.2	15	10	0.2-0.4	10	76	42
RDS	0.3	207	0.5	12.5	15	0.5-1	7	10	5
HRI	0.1	1000	0.2	12.5	5	0.2-0.4	2	7	5

^a cf. text for explanation of acronyms

^b approximate, in square degrees

^c PSPC exposure time, in ksec

^d quoted limiting flux $S(0.5 - 2\text{keV})$ in units of $10^{-14} \text{ erg cm}^{-2} \text{ s}^{-1}$

^e maximum off-axis angle in survey in arcmin

^f radius of error circle searched in survey in arcsec

^g flux range for which FC, FL and FU have been estimated

^h percentage FC of contaminated objects

ⁱ percentage FL of lost objects

^j percentage FU of unidentifiable objects

by the source counts. As a best guess for the resolved fraction we take 70 – 80%.

7.3. Comparison to shallower PSPC surveys

The optical identifications in the *Lockman Hole* and the detailed comparison with other work is described in paper II (Schmidt et al., 1997). Here we want to draw global comparisons with other PSPC surveys, in particular applying the simulation results described above. Quite a number of groups are involved in optical identifications of deep and medium-deep survey fields observed with ROSAT (see Table 6) and already many papers have been written about the interpretation of ROSAT survey results. Among the most debated findings is the claimed detection of a possible new class of X-ray active, optically relatively normal emission line galaxies at faint flux levels (Griffiths et al., 1996, McHardy et al., 1997). Unfortunately, however, only very few surveys so far have been published formally (i.e. including a catalogue of detected sources and a detailed description of the detection and identification procedure), so that quantitative comparisons can be made. Among those published are the Cambridge-Cambridge ROSAT Serendipity Survey (CRSS, Boyle et al., 1995), a small part of the deep ROSAT survey (DRS, Shanks et al., 1991, see also Georgantopoulos et al., 1996) and the North Ecliptic Pole Survey (NEP, Bower et al., 1996). Among those waiting to be fully published are the ROSAT International X-ray Optical Survey (RIXOS, Mason et al., in prep., see also Page et al., 1996), the UK ROSAT deep field survey (UKDS, McHardy et al., 1997), the full DRS, the survey in the Marano field (MARA, Zamorani et al., in prep.), and

finally our own ROSAT Deep Survey (RDS, this paper; Schmidt et al., 1997). Nevertheless, the global properties of these surveys are known and some details can be obtained from the existing literature. See Table 6 for a summary of the surveys in question. The table also includes a prediction for the HRI ultradeep survey.

Using the experience gained from the ROSAT Deep Survey and applying the simulation tools to the shallower surveys we can now make some statements about the expected quality of the other surveys, in particular with respect to possible confusion and the corresponding optical misidentification. As we have seen in Table 5, various confusion problems, as indicated by the FL, FC and FU percentages, become severe roughly within a factor of 2 from the formal detection threshold of a PSPC exposure longer than 50 ksec. It is interesting to note that this behaviour is not a strong function of the exposure time. In order to obtain a more quantitative assessment of the different surveys, we use our PSPC simulations of 50 ksec (DRS, MARA), 110 ksec (UKDS) and 200 ksec (RDS) exposures applying as far as possible the detailed information about exposure times, quoted flux limit, off-axis angles and assumed error circle radii in the individual surveys (see Table 6). For the 80 ksec NEP survey we use quantities interpolated between the 50 ksec and the 110 ksec simulations. For lack of even shallower simulations we do not make statements about the RIXOS and CRSS surveys. For each of the deep and medium-deep surveys in Table 6 we calculate the quantities FC, FL and FU, for a flux range within a factor of two from the sensitivity limit quoted by the authors. This way we can predict for

each survey the fraction of misidentified sources among the faint source population, where presumably the new discoveries would be expected.

It is not surprising to see, that those surveys that employ a relatively conservative limiting sensitivity (as judged from the ratio between exposure time and flux limit) have very small fractions of unidentifiable sources. This is confirmed by the high rate of identifications e.g. for the NEP survey (Bower et al., 1996) and the RDS (Schmidt et al., 1997). The RDS is additionally helped by the HRI data in the field. Larger fractions of unidentifiable sources on the order of 10% are expected for the DRS and the Marano survey. Indeed, in the Marano field, which unfortunately does not have HRI coverage, we see a significant number of empty error boxes (Zamorani et al., in preparation). Unidentified source fractions of order 20% are no major problem as long as one is studying majority populations of X-ray sources (e.g. AGN). They are, however, already a substantial problem if one tries to identify new classes of objects which necessarily are minority classes. There the error can easily approach 100%. For the UKDS, which tried to push deepest in the optical identification, unfortunately the largest unidentifiable fraction (42%) is expected. Indeed, about 26% out of a total of 34 UKDS sources fainter than $5 \times 10^{-15} \text{ erg cm}^{-2} \text{ s}^{-1}$ are unidentified (as derived from Fig. 5 in McHardy et al., 1997), either because the error boxes are empty or contain too faint objects. Judging from our simulations we also expect some of the UKDS sources with proposed optical counterparts to be misidentified.

8. Conclusions

We have presented the complete catalogue of 50 X-ray sources with 0.5–2 keV fluxes above $5.5 \times 10^{-15} \text{ erg cm}^{-2} \text{ s}^{-1}$ from the ROSAT Deep Survey pointing of exposure time 207 ksec in the Lockman Hole. The X-ray positions are largely defined by additional ROSAT HRI observations of more than 1Msec total exposure time. Using the HRI data we have derived a new $\log(N)$ – $\log(S)$ function reaching a source density of $970 \pm 150 \text{ deg}^{-2}$ at a limiting flux of about $10^{-15} \text{ erg cm}^{-2} \text{ s}^{-1}$. At this level 70–80% of the 0.5–2 keV X-ray background is resolved into discrete sources. The observations and the analysis procedure specifically developed to cope with confused X-ray observations have greatly profited from detailed simulations of PSPC and HRI fields. Based on these simulations we have defined conservative limits on flux and on off-axis angles, which guarantee a high reliability of the catalogue. The fraction of confused or unidentifiable sources in the catalogue is expected at only a few percent, but is probably even lower due to the existence of the deep HRI data.

We also discussed simulations of shallower fields and show that surveys, which are only based on PSPC exposures larger than 50 ksec, become severely confusion limited typically a factor of 2 above their 4σ detection

threshold. Sizeable fractions of confused and unidentifiable sources are expected for some of the published surveys. This may have consequences for some recent claims of a possible new source population emerging at the faintest X-ray fluxes.

Acknowledgements. The ROSAT project is supported by the Bundesministerium für Forschung und Technologie (BMFT), by the National Aeronautics and Space Administration (NASA), and the Science and Engineering Research Council (SERC). This work was supported in part by NASA grants NAG5–1531 (M.S.), NAG8–794, NAG5–1649, and NAGW–2508 (R.B. and R.G.). G.H. acknowledges the grant FKZ 50 OR 9403 5 by the Deutsche Agentur für Raumfahrtangelegenheiten (DARA). G.Z. acknowledges partial support by the Italian Space Agency (ASI) under contract ASI 95–RS–152.

References

- Barcons X., Branduardi-Raymont G., Warwick R.S., et al., 1994, MNRAS 268, 833
- Bower R. G., Hasinger G., Castander F. J., et al., 1996, MNRAS, 281, 59
- Boyle B.J., Griffiths R.E., Shanks T., et al. 1993, MNRAS 260, 49
- Boyle B.J., Shanks T., Georgantopoulos I., et al., 1994, MNRAS 271, 639
- Boyle B.J., McMahon R.G., Wilkes B.J., Elvis M., 1995, MNRAS 272, 462
- Branduardi-Raymont G., Mason K.O., Warwick R.S. et al., 1994, MNRAS 270, 947
- Cagnoni I., Della Ceca R., Maccacaro T., 1997, ApJ (submitted)
- Cash W., 1979, ApJ 228, 939
- Chen L.-W., Fabian A.C., Gendreau K.C., 1997, MNRAS 285, 449
- Comastri A., Setti G., Zamorani G., Hasinger G., 1995, A&A 296, 1
- David F.R., Harnden Jr. F.R., Kearns K.E., et al., 1996, in: The ROSAT Users Handbook, Briel et al., eds.
- Gendreau K.C., Mushotzky R., Fabian A.C., et al., 1995, PASJ 47, L5
- Georgantopoulos I., Stewart G.C., Shanks T., et al., 1996, MNRAS, 280, 276
- Giacconi R., Gursky H., Paolini F. R., Rossi B. B., 1962, Phys. Rev. Lett., 9, 439
- Giacconi R., Bechtold J., Branduardi G., et al. 1979, ApJ 234, L1
- Gioia I., Maccacaro T., Schild R.E., et al. 1979, ApJS 72, 567
- Griffiths R.E., Murray S.S., Giacconi R., et al. 1983, ApJ 269, 375
- Griffiths R.E., Della Ceca R., Georgantopoulos I., et al., 1996, MNRAS, 281, 71
- Hamilton T.T., Helfand D.J., Wu X., 1991, ApJ 379, 576
- Hasinger G., 1996, IAU Symp. 168, 245
- Hasinger G., Burg R., Giacconi R. et al., 1993, A&A 275, 1 (erratum A&A 291, 348) (H93)
- Hasinger G., Johnston H., Verbunt F., 1994a, A&A 288, 466
- Hasinger G., Boese G., Predehl P., et al., 1994b, Legacy 4, 40, MPE/OGIP Calibration Memo CAL/ROS/93–015

- Inoue H., Kii T., Ogasaka Y., et al., 1996, in in *Röntgenstrahlung from the Universe*, H.-U. Zimmermann, J. Trümper, H. Yorke, eds., MPE report 263, p. 323
- Jones L.R., McHardy I.M., Merrifield M.R. et al., 1996 MNRAS submitted (astro-ph/9610124)
- Lockman F.J., Jahoda K., McCammon D., 1986, ApJ 302, 432
- McHardy I.M., Jones L.R., Merrifield M.R. et al., 1997 MNRAS submitted (astro-ph/9703163)
- Page M.J., Carrera F.C., Barcons X. et al., 1996, MNRAS 281, 579
- Pfeffermann E., Briel U.G., 1992, IEEE Trans. Nucl. Sci., vol. 39, no. 4, p.976
- deRuiter H.R., Zamorani G., Parma P. et al., 1997, A+A 319, 7
- Schmidt M., Hasinger G., Gunn J., et al., 1997, A&A, in press (Paper II)
- Shanks T., Georgantopoulos I., Stewart G.C., et al. 1991, Nature 253, 315
- Voges W., 1992 in: Proc. ESA ISY Conference, ESA ISY-3, p.9
- Voges W., Aschenbach B., Boller T., et al., 1996, IAU Circ. 6420
- Williams R.E., Blacker B., Dickinson M., et al., 1996, AJ 112, 1335
- Zdziarski A.A., 1996, MNRAS 281, L9
- Zimmermann H.U., Becker W., Belloni T., et al., 1994, MPE report 257